Sparse Ultrasound Image Reconstruction From a Shape-Sensing Single-Element Forward-Looking Catheter

Jovana Janjic, Frits Mastik, Merel D. Leistikow, Johan G. Bosch, *Member, IEEE*, Geert Springeling, Antonius F. W. van der Steen, *Fellow, IEEE*, and Gijs van Soest

Abstract*—*Objective: **Minimally invasive procedures, such as intravascular and intracardiac interventions, may benefit from guidance with forward-looking (FL) ultrasound. In this work, we investigate FL ultrasound imaging using a single-element transducer integrated in a steerable catheter, together with an optical shape sensing (OSS) system.** ***Methods:*** **We tested the feasibility of the proposed device by imaging the surface of a tissue-mimicking (TM) phantom and an *ex vivo* human carotid plaque. While manually steering the catheter tip, ultrasound A-lines are acquired at 60 Hz together with the catheter shape from the OSS system, resulting in a two-dimensional sparse and irregularly sampled data set. We implemented an adaptive Normalized Convolution (NC) algorithm to interpolate the sparse data set by applying an anisotropic Gaussian kernel that is rotated according to the local direction of the catheter scanning pattern. To choose the Gaussian widths tangential (σ_t) and normal (σ_n) to the scanning pattern, an exhaustive search was implemented based on RMSE computation on simulated data.** ***Results:*** **Simulations showed that the sparse data set contains only 5% of the original information. The chosen widths, $\sigma_n = 250\ \mu$m and $\sigma_t = 100\ \mu$m, are used to successfully reconstruct the surface of the phantom with a contrast ratio of 0.9. The same kernel is applied successfully to the carotid plaque data.** ***Conclusion:*** **The proposed approach enables FL imaging with a single ultrasound element, mounted on a steerable device.** ***Significance:*** **This principle may find application in a variety of image-guided interventions, such as chronic total occlusion (CTO) recanalization.**

***Index Terms*—Ultrasound, IVUS, optical shape sensing, normalized convolution, chronic total occlusion.**

Manuscript received October 22, 2017; revised December 15, 2017; accepted December 20, 2017. Date of publication January 18, 2018; date of current version September 18, 2018. This work was supported in part by the Dutch Technology Foundation STW under Grant 12710, which is a part of the Netherlands Organization for Scientific Research, which is partly funded by the Ministry of Economic Affairs. *(Corresponding author: Jovana Janjic.)*

J. Janjic is with the Department of Biomedical Engineering, Thoraxcenter, Erasmus MC, Rotterdam 3000 CA, The Netherlands (e-mail: j.janjic@erasmusmc.nl).

F. Mastik, J. G. Bosch, A. F. W. van der Steen, and G. van Soest are with the Department of Biomedical Engineering, Thoraxcenter, Erasmus MC.

M. D. Leistikow is with the Philips Research Europe, In-Body Systems, High Tech Campus.

G. Springeling is with the Department of Experimental Medical Instruments, Erasmus MC.

Digital Object Identifier 10.1109/TBME.2017.2787060

I. Introduction

FORWARD-LOOKING (FL) ultrasound catheters can provide guidance during minimally invasive procedures, such as recanalization of arterial chronic total occlusion (CTO). In such cases, an atherosclerotic plaque has grown to completely block the vessel. Conventional intravascular ultrasound (IVUS) imaging in a side-looking geometry is of limited use. CTOs are complex lesions with heterogeneous tissue composition consisting of lipids, organized thrombus, calcium and collagen-rich fibrous tissue [1]. They can develop in the relatively small coronary arteries, but also in the larger peripheral arteries. In order to aid the CTO crossing procedure, FL ultrasound may provide useful information, such as the best entry point or local tissue composition [2], [3]. Forward-looking transducers may be beneficial for other applications as well, such as intracardiac echography for the diagnosis of cardiac arrhythmias [4], [5], or guidance during transjugular intrahepatic portosystemic shunt (TIPS) procedures, where a shunt is created in the liver to decrease the high blood pressure in patients with portal hypertension [6], [7] and the portal vein needs to be located under image guidance.

Catheter-based FL ultrasound technology is still in development and several concepts have been pursued in experimental settings. Early work explored single element transducers mounted on a rotating cam assembly [8], [9]. This mechanism is rather complex and makes the whole catheter bulky and unstable. In other studies, linear transducer arrays have been investigated as a way to provide 2D imaging ahead of the catheter tip without mechanical scanning [10], [11]. The major problems with this approach are the limited space available and the constraints in PZT fabrication that make the integration into catheters very challenging. Capacitive micromachined ultrasonic transducers (CMUT) offer a great advantage in terms of fabrication over PZT since very small dimensions and arbitrary geometries of the elements can be achieved using lithography techniques and micro-fabrication processes [12]. This technology has been used by several groups in the attempt of developing catheter-based FL ultrasound transducers [5], [13]–[17]. However, integration and miniaturization of electronics remains the major problem.

In this work, we propose an alternative approach to achieve FL ultrasound imaging by integrating three components in one

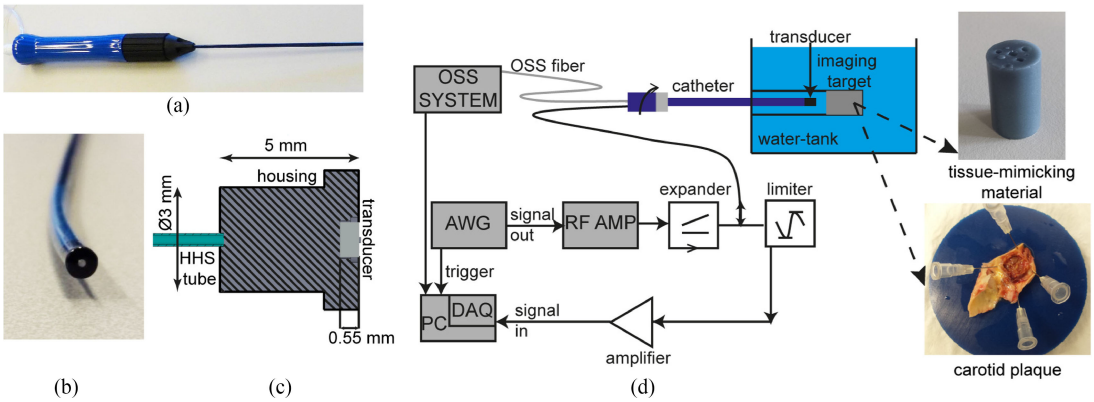

Fig. 1. (a) Handle of the steerable catheter (MobiCath, Biosense Webster), (b) tip of the steerable catheter with the single element transducer (inner gray circle), (c) schematic drawing of the transducer housing with the HHS tube for the OSS fiber, and (d) the measurement set-up, with TM phantom and carotid plaque.

device: a single-element ultrasound transducer, an optical shape sensing (OSS) fiber and a catheter that can be steered along two directions in one plane. While steering the catheter, single ultrasound A-lines can be acquired at different locations together with the catheter 3D shape obtained from the OSS data. Having a single-element transducer reduces the complexity of integration, whereas the position and direction information from the OSS data allow to combine the individual A-lines in 3D space. This paper builds on an earlier initial work by our group to integrate a similar device with preliminary results on target reconstruction [18], [19].

Since the steering is performed manually and is limited to specific patterns due to the catheter design, a sparse and irregularly sampled data set is obtained. To reconstruct FL images of the target from sparse data, an interpolation algorithm is required. In previous works different approaches to sparse image reconstruction have been proposed [20], [21]. A method that has shown good performance is Normalized Convolution (NC) [22]–[24]. NC takes into account the certainty of the signal and applies a diffusion kernel to fill the empty spaces in the image. We implement an adaptive interpolation method based on NC, where the diffusion kernel changes orientation dynamically depending on the local scanning pattern of the catheter. A similar approach was used in [25] with the difference that there the diffusion kernel was adapting to the image gradient. We tested our adaptive NC method both on simulated and real data, focusing on the reconstruction of the front surface of a tissue mimicking (TM) phantom and of a carotid plaque obtained from endarterectomy.

II. Methods

A. Experimental Configuration

To perform FL ultrasound imaging with a single element transducer on a steerable catheter, we have developed a prototype device based on a commercially available bi-directional steerable guiding sheath (8.5 F, MobiCath, Biosense Webster). The dimensions of this sheath are suitable for peripheral vasculature applications, but exceed the allowable dimension for coronary artery access. By rotating the catheter handle (Fig. 1(a)), the tip can be steered in two directions in one plane and by rotating the entire catheter, the steering plane can be chosen. At the tip of the catheter, which is free from steering cables, we place a single-element ultrasound transducer (Fig. 1(b)). The ultrasound transducer is a circular PZT element with a diameter of 1 mm and 25 MHz center frequency, mounted in a custom-made housing (Fig. 1(c)). The single element transducer can also be mounted on steerable catheters with smaller outer diameter. The transducer is electrically wired with a 160 μm coaxial cable that is guided through the inner lumen of the catheter.

The OSS system (a research prototype developed at Philips Research, Eindhoven, NL) consists of an optical fiber with a diameter of 200 μm, connected to a scanning laser system [18], [26]. The fiber has four inner cores, one along the longitudinal axis and three wound around it in a helical fashion. Fiber Bragg Gratings (FBG), which consist of periodic variation in refractive index, are patterned along the entire length of the fiber (1.8 m). Bends in the fiber induce local stretching and compression of the period of the FBG, allowing measurements of the local strain based on optical reflectometry in the frequency domain [27]. The central wavelength of the scanning laser is set to 1545 nm, and is swept over 17 nm. The spatial resolution along the sensor is 50 micrometer. The 3D shape is obtained by performing a distributed measurement of the applied strain to each of the four cores. By integrating forward along the fiber from the first sensing point, which is fixed in the reference frame, and combining the information from all four cores, the geometry of the sensor can be obtained. Since the position of each sensor point is estimated based on the previous one, the precision of the estimation decreases with increasing length of reconstruction. Additional details about the working principle can be found in [26], [27]. A helical hollow strand (HHS) tube (0.5 mm in diameter) protects the OSS fiber. The HHS tube is guided through the catheter lumen and one end is attached to the back of the transducer housing, whereas the other end is accessible to insert the fiber.

We simultaneously acquire OSS data and US data while steering the catheter. A 2-cycle sinusoidal pulse at 40 Vpp with a

center frequency of 25 MHz is sent to the transducer using a waveform generator (Tektronix, 3102) and an RF power amplifier (ENI, 310L), whereas the received signal is amplified by 40 dB (Hewlett-Packard, 461A) and digitized with a sampling frequency of 350 MHz (Acqiris, DP310). The OSS data are acquired at 60 Hz via the user interface developed by Philips, providing the total shape and curvature of the fiber. A Matlab script provides a real time feedback of the covered area by plotting the catheter tip coordinates in 2D and the corresponding ultrasound A-lines. Further signal processing and image reconstruction are performed off-line in Matlab (R2016a), using a personal computer with an Intel i7-3770, 3.4 GHz, 4-core processor. Fig. 1(d) shows a schematic of the complete set-up used in our measurements. The imaging target is submerged in a water tank into which the steerable catheter is inserted from the side of the tank, clamped using an O-ring and guided into a plastic tube that confines and limits its movements.

As imaging target we used a tissue mimicking (TM) phantom and an ex vivo human carotid plaque (Fig. 1(d)). The agar-based phantom has a cylindrical geometry with a diameter of 16 mm and has hollow channels running through the total length and steel spheres embedded at the surface. The ex vivo human carotid plaque is obtained following endarterectomy procedures, under a research protocol sanctioned by the Medical Ethics Committee of the Erasmus Medical Center MC (MEC-2008-174). The human specimen was snap frozen in liquid nitrogen within 10–20 min following endarterectomy and stored at 80°. The tubular specimen was then thawed, cut open along the longitudinal axis, mounted on a rubber support and submerged in saline solution with the inner plaque layer facing the ultrasound probe. A 3D ultrasound image of the plaque was obtained as ground truth using a high frequency pre-clinical ultrasound scanner operated at 21 MHz (Vevo 2100 with MS250, VisualSonics Inc., Toronto, ON, Canada). In addition, we scanned the plaque with the 25 MHz single element transducer clamped to a positioning stage and mechanically scanned along a regular grid pattern with a step size of 100 μm in both x and y directions.

B. Ultrasound Data Processing

Each ultrasound A-line is filtered in Matlab using a Butterworth filter of order 5 with a bandwidth between 15 MHz and 45 MHz. After filtering, the envelope is computed using the Hilbert transform. We focus on the reconstruction of the surface of TM phantoms with high-intensity hard spots and low-intensity channels and on visualization of the surface of the carotid plaque. The surface is obtained from the ultrasound A-lines by intensity thresholding: for each A-line, if the signal is above the noise level, we consider the corresponding distance value as the surface location. The noise level was measured considering the average signal in the water region before the surface of the phantoms. For points where we do not find a distance value, like the phantom channels, we linearly interpolate between known neighbors. Next, we consider the envelope signal corresponding to a 400 μm thick slice of the imaged object starting from the surface and we project the envelope mean values on a 2D plane based on the tip position and direction obtained from the OSS system and based on the tip-to-target distance computed with ultrasound. At the same time, we also store the tip-to-target distance for each tip position. When computing the tip-to-target distance we apply an offset of 5 mm to take into account that the OSS fiber tip is not exactly at the same axial location as the transducer (see Fig. 1(c)). The resulting 2D data sets form two sparse and irregularly sampled maps: one for the subsurface intensities and one for the tip-to-target distances.

C. Estimation of Catheter Tip Position and Direction

For each acquired data set, the 3D coordinates of the sensing points along the fiber and their curvature are provided by the OSS system. We use the curvature plot of each fiber shape to find the point that corresponds to the location where the catheter is clamped to the side of the water tank. At this location, a peak in the curvature is visible, due to the deformation applied by the clamping mechanism. Knowing that the clamping point is not moving, we can use it as a new reference point and reduce the reconstructed length of the fiber, thus decreasing the error in position estimation. Next, we compute the catheter tip position and direction relative to the new reference point. The obtained coordinates are further smoothed applying a spline fit in order to obtain a more regular scanning pattern and remove possible outliers.

D. Sparse Data From Simulated Target

To simulate a sparsely sampled data test, we use a measured scanning pattern obtained from one of the OSS acquisitions and simulate an imaging target in a plane perpendicular to the mean direction of the catheter tip, at a distance of 4 mm. The simulated target consists of a regular grid of holes and strong reflectors (Fig. 2(a)). To simulate a target that is sampled by an ultrasound transducer, we convolve the target image with the ultrasound transducer point spread function (PSF) at 4 mm (Fig. 2(b)), which has a -3-dB diameter of approximately 500 μm. An image of the target after PSF application is shown in Fig. 2(c). We sample the simulated target after PSF application by projecting the catheter tip position on the target plane.

E. Image Reconstruction with Adaptive Normalized Convolution (NC)

NC is a technique used for interpolation of sparse, irregularly sampled data based on their certainty by applying a predefined diffusion kernel [22]–[24]. More in detail, considering a sparse image S and its certainty map C, the normalized convolution result R is obtained as follows:

$$\mathrm{R} = \frac{(\mathrm{S} \cdot \mathrm{C}) \otimes \mathrm{G}}{\mathrm{C} \otimes \mathrm{G}} \tag{1}$$

where G is the diffusion kernel and $\otimes$ indicates convolution. The certainty map represents the certainty for the image samples, which is 1 for each sampled position and 0 everywhere else. The diffusion kernel is usually represented by the 2D Gaussian

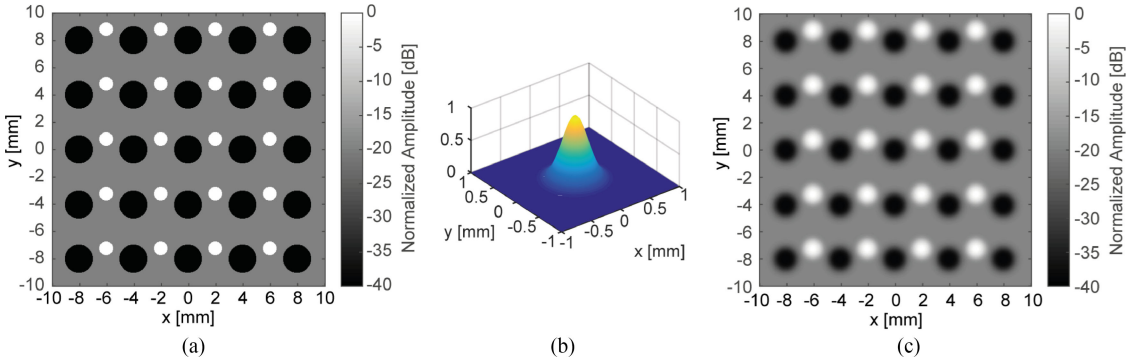

Fig. 2. (a) Simulated imaging target consisting of a regular grid of holes and strong reflectors, (b) ultrasound PSF at 4 mm, (c) imaging target convolved with the ultrasound PSF at 4 mm.

function

$$\mathrm{G}\left(\mathrm{x},\mathrm{y}\right)=\exp\left[-\left(\frac{\mathrm{x}}{\sigma_{\mathrm{x}}}\right)^{2}-\left(\frac{\mathrm{y}}{\sigma_{\mathrm{y}}}\right)^{2}\right] \tag{2}$$

where the parameters σ_{x} and σ_{y} represent the width of the kernel in the x and y direction, respectively. In conventional NC the diffusion kernel is an isotropic Gaussian, with $\sigma_{\mathrm{x}}=\sigma_{\mathrm{y}}$.

In our study, the sparsely sampled data obtained from both the simulations and the real measurements are used to generate a sparse matrix image with a pixel size of $40\times 40\,\mu$m. In the simulations the sparse image S contains the intensity values sampled using a measured scanning patterns obtained from one of the OSS acquisitions. For the real measurements, beside the intensity sparse map, we also define the sparse map of the tip-to-target distances. Therefore, during the scan, we accumulate the amplitude values per pixel in S_i and the distance values per pixel in S_d while keeping track of the number of measurements in each pixel of C. As diffusion kernel we apply an anisotropic Gaussian function that is rotated according to the local scanning pattern of the steerable catheter. The idea is to diffuse the sparse intensity map, the sparse distance map and the certainty map taking into account that we have a very dense sampling along the scanning path and a very sparse sampling in the other directions. The dense sampling along the scanning path is due to the high sampling rate (60 Hz) combined with the slow motion of the catheter (approximately 0.6 mm/s). More in detail, the adaptive diffusion kernel is defined as

$$\begin{aligned}\mathrm{G}\left(\mathrm{x}_{\theta},\mathrm{y}_{\theta}\right)&=\exp\left[-\left(\frac{\mathrm{x}_{\theta}}{\sigma_{\mathrm{t}}}\right)^{2}-\left(\frac{\mathrm{y}_{\theta}}{\sigma_{\mathrm{n}}}\right)^{2}\right]\ \text{with}\ \left(\mathrm{x}_{\theta},\mathrm{y}_{\theta}\right)\\&=\left(\mathrm{x},\mathrm{y}\right)\cdot\begin{bmatrix}\cos\theta & \sin\theta\\ -\sin\theta & \cos\theta\end{bmatrix}\end{aligned} \tag{3}$$

where σ_{t} represents the width of the kernel along the direction tangential to the path, σ_{n} represents the width of the kernel along the direction normal to the path and θ is the angle between the direction normal to the path and the x axis of the image. A schematic drawing is shown in Fig. 3. Both the sparse map S (intensities and distances) and the certainty map C are locally convolved with the adaptive kernel following (1) and the resulting diffused maps are divided to obtain the adaptive NC result

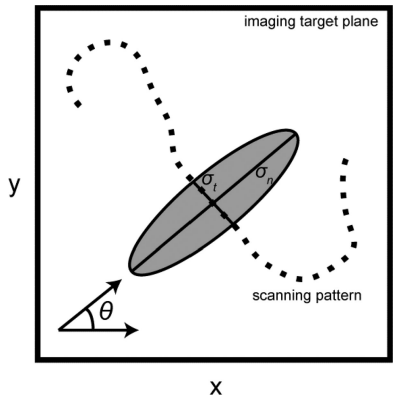

Fig. 3. Schematic drawing of a scanning pattern (dotted line) on the imaging target plane with a rotated anisotropic kernel (gray area). Dotted line represents the scanning path, gray ellipsoid represents the diffusion kernel; $\sigma_{\mathrm{t}}=$ width of the kernel along the direction tangential to the path, $\sigma_{\mathrm{n}}=$ width of the kernel along the direction normal to the path, $\theta=$ angle between the direction normal to the path and the x axis of the image.

for both the intensities and the distances. To find the optimal parameters for σ_t and σ_n we perform an exhaustive search using the simulated sparse intensity data. Both σ_t and σ_n are varied between 50 and 500 μm and, for each possible combination of parameters, the adaptive NC result is computed. The obtained image $\mathrm{I}_{\mathrm{aNC}}$ is compared to the simulated ground truth image $\mathrm{I}_{\mathrm{truth}}$ (Fig. 2(a)) by computing the root-mean-square error on the linear intensities as:

$$\mathrm{RMSE}=\sqrt{\frac{1}{N_{\mathrm{pixel}}}\sum_{\mathrm{n}=0}^{N_{\mathrm{pixel}}-1}\left(I_{\mathrm{aNC}}\left(\mathrm{n}\right)-I_{\mathrm{truth}}\left(\mathrm{n}\right)\right)^{2}} \tag{4}$$

The values of the parameters σ_{t} and σ_{n} for which we get a low RMSE, are then used in the adaptive NC to reconstruct the image of the simulated target, the TM phantom and the carotid plaque. For the TM phantom we apply adaptive NC with different combinations of parameters σ_{t} and σ_{n}, and we compute the contrast ratio CR, which is defined as [28]

$$\mathrm{CR}=\frac{\mu_{\mathrm{b}}-\mu_{\mathrm{c}}}{\mu_{\mathrm{b}}+\mu_{\mathrm{c}}} \tag{5}$$

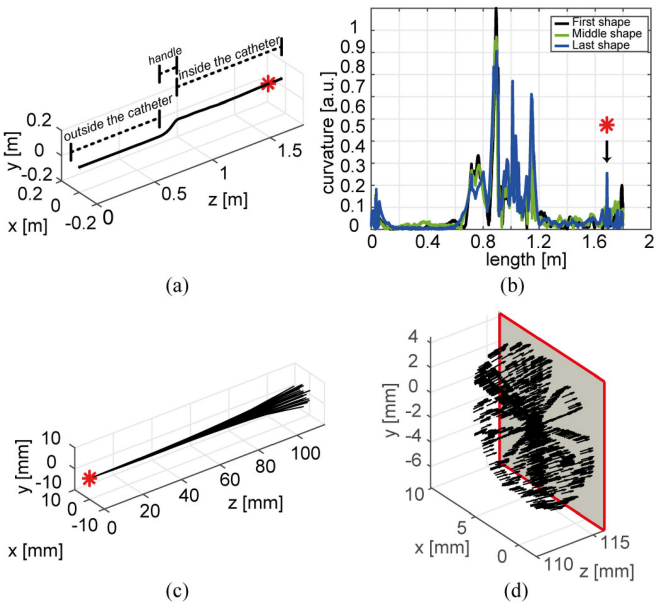

Fig. 4. (a) A representative 3D shape of the fiber inserted into the steerable catheter; (b) curvature plot for three different shapes: first, middle and last shape during one measurement; (c) 3D shapes of the last 10 cm of the steerable catheter during one measurement, (d) Catheter tip position and direction (black arrows) in 3D. The gray plane delineated by red lines indicates the imaging plane. The red asterisk indicates the location at which the catheter has been clamped to the side of the water tank.

where μ_b is the average signal amplitude from the tissue-mimicking material and μ_c is the average signal amplitude in the hollow channel region.

III. Results

Fig. 4(a) shows a typical 3D reconstruction of the entire OSS fiber, including the portion integrated into the steerable catheter, which is clamped at the side of the water tank. The z-axis of the 3D shape reconstruction corresponds to the catheter long axis. Fig. 4(b) shows the curvature of three different shapes acquired while manually scanning the catheter. The three curvature plots are representative of the initial, intermediate and final shape of the catheter during one acquisition. The curvature peaks around 0.9 m coincide with the catheter handle location, whereas the peak indicated by the red mark corresponds to the location at which the catheter has been clamped to the side of the water tank. Since only the tip of the catheter is steering, we use the catheter clamping point as a new reference point for the OSS reconstruction. Fig. 4(c) shows the shapes of approximately the last 10 cm of the catheter during one acquisition, whereas Fig. 4(d) shows the tip position and direction after spline filtering. The results presented in the following sections where achieved with a non-optimized algorithm that computes the adaptive kernel at a rate of 68 data points (tip positions with corresponding intensities) per second. Since each acquisition contains 15000 tip positions and relative ultrasound intensities, the final adaptive NC images were computed in 3 min and 40 sec.

A. Adaptive Normalized Convolution on Simulated Data: Optimal Parameter Choice

The scanning pattern shown in Fig. 4(d) is applied to the simulated target (Fig. 2(c)) to obtain the sparse certainty and sparse intensity maps of Fig. 5(a) and (b). In the resulting map, only 5% of the original image information is retained. Fig. 5(d)–(f) show the conventional NC steps where an isotropic Gaussian kernel is applied with $\sigma_x = \sigma_y = 400$ μm. The original simulated imaging target is also shown as a reference (Fig. 5(c)). The optimal parameters σ_t and σ_n for the adaptive NC are found utilizing an exhaustive search. The RMSE for the different combination of parameters is shown in Fig. 5(g). The chosen parameter combination is indicated by the white star and corresponds to $\sigma_n = 250$ μm and $\sigma_t = 100$ μm. The anisotropic kernel with the optimal parameters is applied to the sparse data resulting in the adaptive NC reconstruction shown in Fig. 5(i).

B. Adaptive Normalized Convolution on Phantom Data

An example of ultrasound data obtained from the TM phantom during one measurement is shown in Fig. 6. The data are shown after filtering and after envelope detection. The red line indicates the phantom surface. From the ultrasound A-lines shown in Fig. 6 it is possible to see the gaps in the signal corresponding to the hollow channels (indicated by the yellow solid arrows) and strong reflections corresponding to the steel spheres embedded at the surface (indicated by the yellow dashed arrows).

The average amplitude for each A-line over a depth of 400 μm from the phantom surface is mapped to a 2D plane representing the phantom surface, knowing the tip-to-target distance based on ultrasound and the tip position and direction in 3D based on the OSS data. The resulting average intensity image is shown in Fig. 7(b). Fig. 7(c) shows the corresponding adaptive NC result images with the chosen kernel parameters $\sigma_n = 250$ μm and $\sigma_t = 100$ μm. Both average intensity image and adaptive NC images are shown with a dynamic range of 40 dB. Next, we apply the adaptive NC reconstruction on the tip-to-target distance (Fig. 7(d)) and, by combining the distance and intensity reconstructions, we obtain the surface plot shown in Fig. 7(e), with most of the intensity values located in one plane, in agreement with the fact that the front surface of the phantom is flat. To confirm the improved contrast obtained by applying adaptive NC with the chosen parameters over standard NC, we compute the contrast ratio for images obtained applying adaptive NC with different combinations of parameters σ_n and σ_t. The result is shown in Fig. 7(f), demonstrating that our choice of σ_n and σ_t lies in the region of highest contrast ratio. In fact, we achieved a contrast ratio equal to 0.9 by using an adaptive Gaussian kernel with $\sigma_n = 250$ μm and $\sigma_t = 100$ μm.

C. Adaptive Normalized Convolution on Carotid Plaque Data

Fig. 8(a) shows the area of the carotid plaque that was imaged and scanned. The yellow arrows indicate the location of calcified

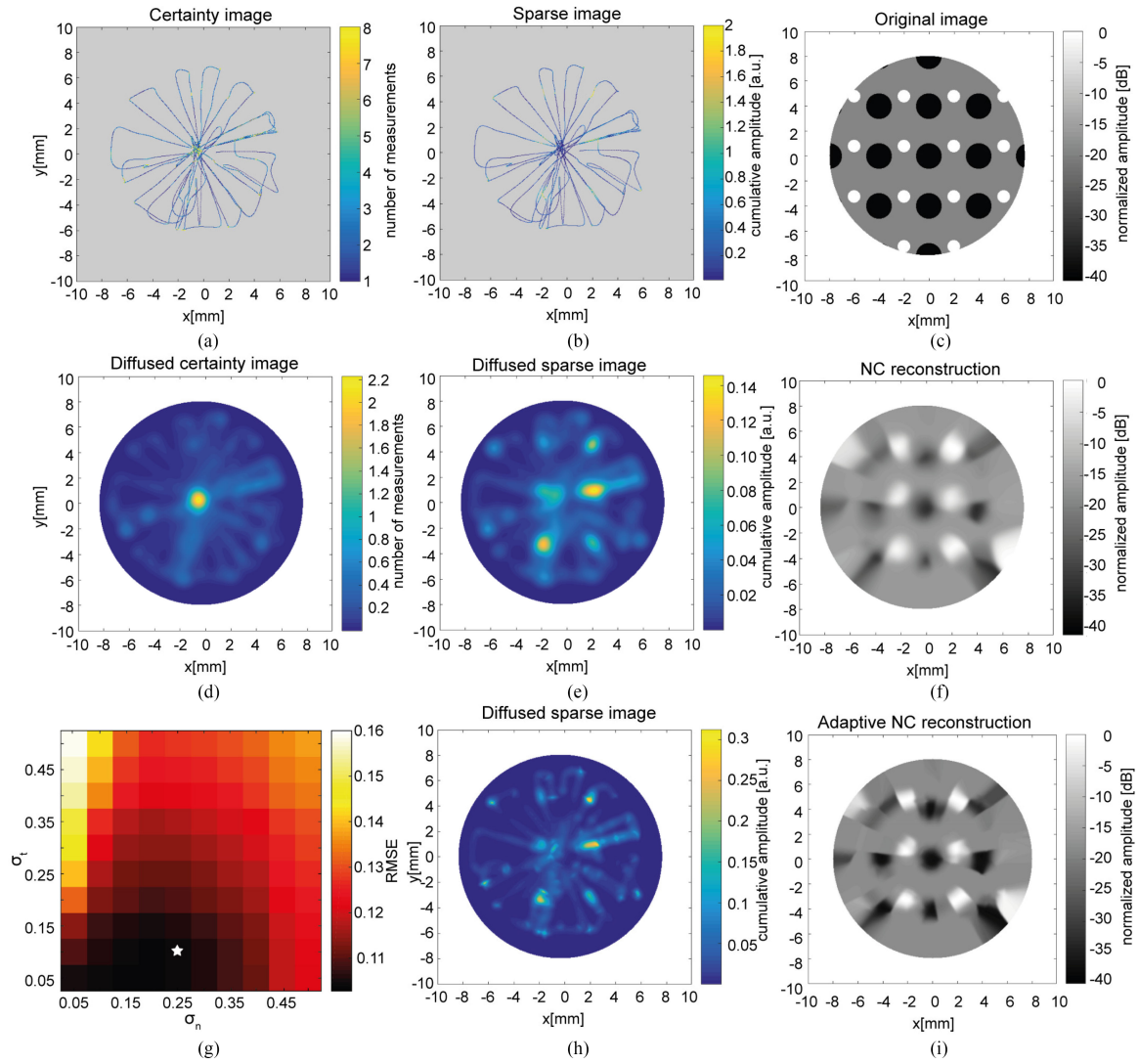

Fig. 5. Standard NC: (a) simulated certainty image and (b) sparse intensity image, both with maximum value clipped for better visibility; (c) original image; (d) diffused certainty image and (e) diffused intensity image using an isotropic kernel with $\sigma_x = \sigma_y = 400$ μm; (f) NC result; (g) RMSE based on linear intensities resulting from the exhaustive search for the NC parameters σ_n and σ_t. The white star indicates the chosen combination of parameters; (h) sparse intensity image diffused with the anisotropic kernel; (i) adaptive NC reconstruction.

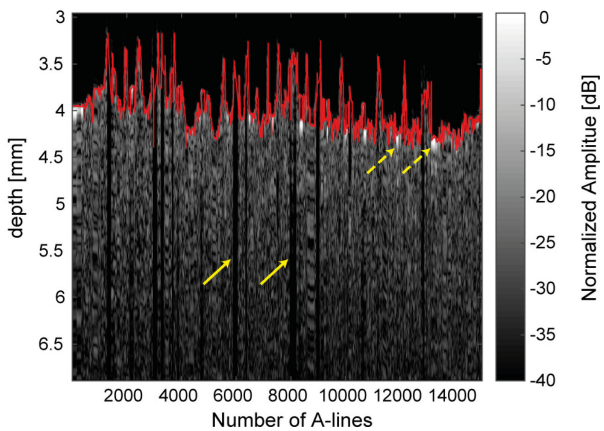

Fig. 6. Ultrasound A-lines obtained by scanning the transducer across the surface of one of the TM phantoms. The red line indicates the phantom surface, the yellow solid arrows indicate some hollow channels and the yellow dashed arrows indicate some strong steel reflectors.

areas. The surface plot obtained with the Vevo 2100 pre-clinical ultrasound scanner is shown in Fig. 8(b). Fig. 8(c) shows the image obtained by scanning the 25 MHz single element transducer over a regular grid pattern mechanically translating the transducer. Fig. 8(d) shows the sparse distance map, whereas Fig. 8(e) shows the intensity sparse map. Both the sparse maps are obtained by manually steering the catheter with the 25 MHz transducer at the tip and acquiring OSS data, similarly to the TM phantom measurements. The result of applying the adaptive NC on both the tip-to-target distances and on the intensity values is shown in Fig. 8(f).

IV. Discussion

In this paper, we have introduced a novel approach to catheter-based FL ultrasound imaging using a single element transducer integrated into a clinically available steerable catheter together with an OSS system. We also have demonstrated that adaptive

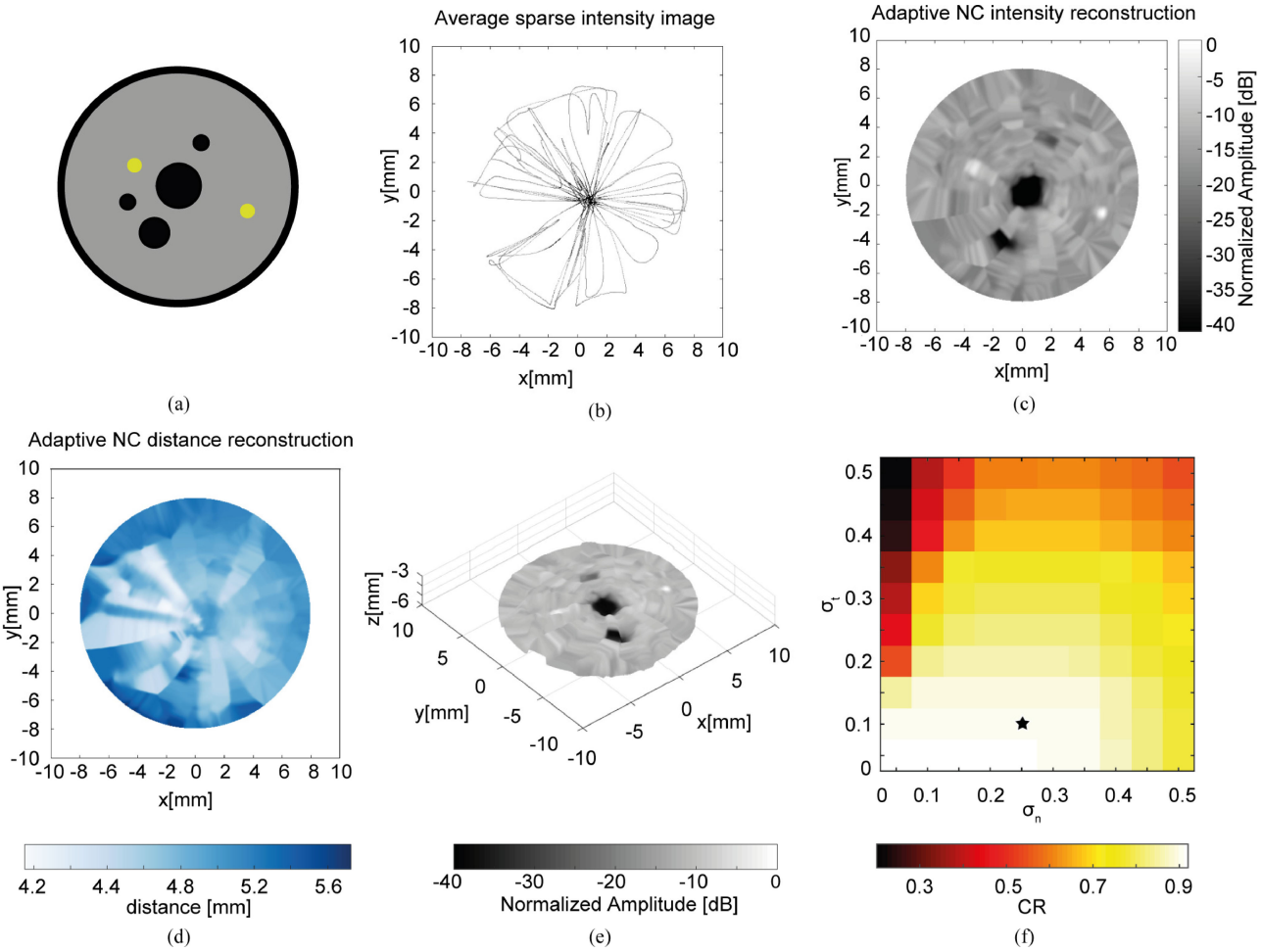

Fig. 7. (a) Schematic drawing of the phantom surface; (b) average sparse intensity image; (c) adaptive NC reconstruction of the intensity; (d) adaptive NC result on the tip-to-target distances; (e) surface plot combining the intensity and distance information; (f) Image contrast ratio obtained using adaptive NC with different combinations of σ_n and σ_t for the TM phantom. The chosen combination of parameters is indicated with a black star.

NC is successful in interpolating the sparse and irregularly sampled data obtained by manually scanning the catheter. A single element catheter is much simpler to build and use than a multi-element one, evidenced by [5], [10], [13]–15]. The only additional component needed to combine the different A-lines is the OSS fiber, which fits easily in the catheter along the transducer coaxial cable, due to its small outer diameter.

The device used in this study has an outer diameter of 4 mm, which makes it suitable for peripheral vascular interventions, such as CTO recanalization. The localization of the channels relative to the calcified regions in the plaque is important during CTO revascularization, since it can point the physician towards the best entry point, shortening the procedure and reducing the risk of complications, such as vessel perforation. In principle, both the transducer and the OSS fiber can be integrated in smaller catheters, such as those used in coronary artery interventions. However, the realization of steerable coronary catheters remains a major challenge.

We combined lateral steering and rotation, resulting in a very high spatial sampling in the central region, but very sparse sampling elsewhere (Fig. 4(d)). The catheter used in this study is a clinically available device. Since the proposed method should be readily applicable to real patient data, using a state of the art catheter ensures easier translation of this novel concept into the clinics. More agile steerable devices may produce sampling patterns with different characteristics. We applied our experimental scan pattern to the simulated image, retaining only 5% of the original image, which further proves the steering limitation of our device.

Despite the limited information available, NC with isotropic kernel reconstructs the major features of the image as shown in Fig. 5(f). However, using an isotropic kernel does not take into account the large difference in sampling density along the path compared to the transverse direction, which results in muted image contrast. Using an adaptive anisotropic Gaussian kernel the major features of the simulated target and the TM phantom are reconstructed, preserving the edges and reducing the blurring along the scanning path, as shown in Fig. 7(c). This is also confirmed by the CR map in Fig. 7(f), showing that the chosen combination of parameters σ_n and σ_t lays in the region where the highest CR values are obtained. For the phantom and the carotid plaque specimen, we can reconstruct most of

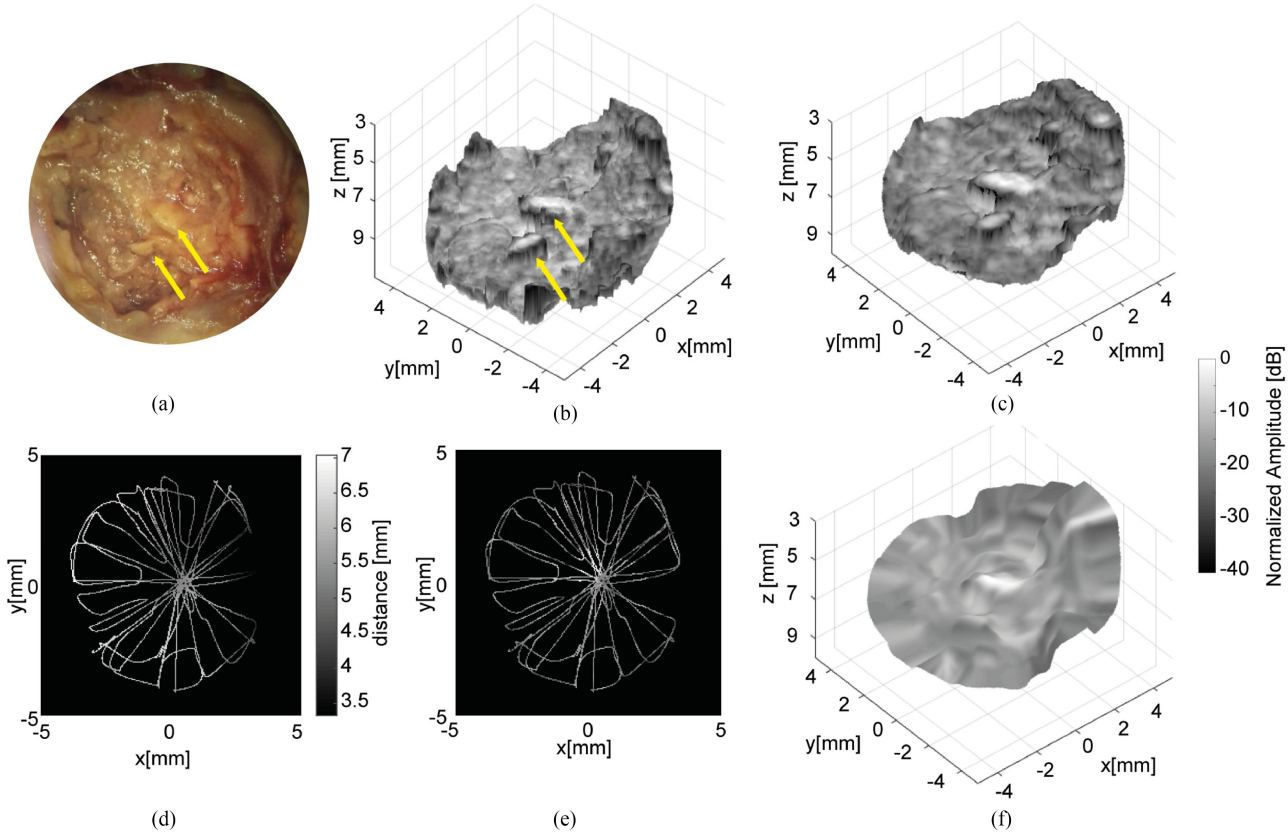

Fig. 8. (a) Picture of the imaged portion of the carotid plaque with yellow arrows indicating calcium; (b) surface reconstruction using the Vevo 2100 scanner with a 21 MHz linear array, (c) surface reconstruction obtained by mechanically scanning the 25 MHz single element transducer on a regular grid pattern; (d) sparse distance map and (e) sparse intensity map obtained by manually scanning the 25 MHz single element transducer mounted on the steerable catheter; (f) surface reconstruction of the after adaptive NC on both the sparse distance and the intensities values.

the features which are not recognizable in the sparse maps. A NC algorithm with adaptive kernel was also used in [25] where the anisotropic kernel was rotated according to the gradient angle of a randomly sampled image. However, in our case, due to the particular scanning pattern and the highly sparse nature of the data, the computation of the gradient is not a suitable choice.

In this work, we have focused on the reconstruction of the imaging target surface by combining the intensity signals and the tip-to-target distance information from ultrasound. For the phantom this results in flat surface reconstruction, whereas in the ex-vivo carotid plaque measurements the surface plot shows the differences in distances for the different structures. The same method can be extended to 3D to reconstruct volumetric images of the structures ahead of the catheter.

The FL ultrasound imaging approach presented in this paper has some limitations. If certain regions of the imaging target are not scanned at all, the reconstructed image will fail in providing information about those regions (see for instance the hole at 8 o'clock in the phantom image). This means that the ability to reconstruct FL images with the proposed device requires the scanning pattern to achieve a certain minimum coverage. Steerable catheters with more flexibility than the one used in this work, as well as random probe motion of which there usually is plenty in (cardiac) interventions, may help in optimizing the coverage of the region of interest.

To reduce the reconstructed length of the fiber, hence decreasing the error in position estimation, we set the reference point to correspond to the clamping point on the side of the water tank. In a clinical setting this will result in moving the reference point within the human body. Since the OSS system provides strain and curvature information over time for each sensing point along the fiber, this information could be used to identify the stable clamping point within the body and set it as reference point.

V. Conclusion

In this work, we have successfully integrated a FL single-element ultrasound transducer in a steerable catheter together with an OSS fiber and we have demonstrated the feasibility of achieving FL imaging. The integrated device acquires ultrasound A-lines and OSS data simultaneously at 60 Hz, while manually steering the catheter tip. The manual scanning leads to a sparse and irregularly sampled data set, which requires interpolation to reconstruct the features at the front surface of the imaging target. We have shown that applying Normalized Convolution with an adaptive anisotropic Gaussian kernel on both the intensity and the distance data enables to generate surface plots of the imaging target. By applying adaptive NC on the phantom data, channels and strong reflectors can be identified, whereas in the carotid plaque image the strong calcified areas are successfully reconstructed.

We have shown that, with only 5% of the original data, it is possible to reconstruct the salient features of the image, such as the location of the channels and the strong reflectors. The chosen combination of adaptive Gaussian parameters, $\sigma_{\mathrm{n}} = 250$ μm and $\sigma_{\mathrm{t}} = 100$ μm, leads to image reconstruction of the phantom surface with a contrast ratio of 0.9.

Acknowledgment

We would like to thank R. H. S. H. Beurskens and M. Manten for the help during the device assembly and integration and K. van Gaalen, F. Gijsen, A. Akyildiz and V. Daeichin for the help with the carotid plaque measurements.

References

[1] G. W. Stone *et al.*, "Percutaneous recanalization of chronically occluded coronary arteries, a consensus document: Part I," *Circulation*, vol. 112, pp. 2364–2372, 2005.

[2] G. W. Stone *et al.*, "Percutaneous recanalization of chronically occluded coronary arteries - A consensus document - Part II," *Circulation*, vol. 112, pp. 2530–2537, Oct. 2005.

[3] B. K. Courtney *et al.*, "Innovations in imaging for chronic total occlusions: a glimpse into the future of angiography's blind-spot," *Eur. Heart J.*, vol. 29, pp. 583–93, Mar. 2008.

[4] M. R. Jongbloed *et al.*, "Clinical applications of intracardiac echocardiography in interventional procedures," *Heart*, vol. 91, pp. 981–90, Jul. 2005.

[5] A. Nikoozadeh *et al.*, "Forward-looking intracardiac ultrasound imaging using a 1-D CMUT array integrated with custom front-end electronics," *IEEE Trans. Ultrason. Ferroelect. Freq. Control*, vol. 55, no. 12, pp. 2651–60, Dec. 2008.

[6] B. Funaki, "Transjugular intrahepatic portosystemic shunt," *Semin. Intervent. Radiol.*, vol. 25, pp. 168–74, Jun. 2008.

[7] Y. Goykhman *et al.*, "Transjugular intrahepatic portosystemic shunt: current indications, patient selection and results," *Isr. Med. Assoc. J.*, vol. 12, pp. 687–91, Nov. 2010.

[8] J. L. Evans *et al.*, "Arterial imaging with a new forward-viewing intravascular ultrasound catheter, I. Initial studies," *Circulation*, vol. 89, pp. 712–7, Feb 1994.

[9] K. H. Ng *et al.*, "Arterial imaging with a new forward-viewing intravascular ultrasound catheter, II. Three-dimensional reconstruction and display of data," *Circulation*, vol. 89, pp. 718–23, Feb. 1994.

[10] D. N. Stephens *et al.*, "Experimental studies with a 9F forward-looking intracardiac imaging and ablation catheter," *J. Ultrasound. Med.*, vol. 28, pp. 207–15, Feb. 2009.

[11] R. Chen *et al.*, "PMN-PT single-crystal high-frequency kerfless phased array," *IEEE Trans. Ultrason. Ferroelect. Freq. Control*, vol. 61, pp. 1033–41, Jun. 2014.

[12] A. F. van der Steen *et al.*, "IVUS beyond the horizon," *EuroIntervention*, vol. 2, pp. 132–42, May 2006.

[13] U. Demirci *et al.*, "Forward-viewing CMUT arrays for medical imaging," *IEEE Trans. Ultrason. Ferroelect. Freq. Control*, vol. 51, pp. 887–95, Jul. 2004.

[14] G. Gurun *et al.*, "Single-chip CMUT-on-CMOS front-end system for real-time volumetric IVUS and ICE imaging," *IEEE Trans. Ultrason. Ferroelect. Freq. Control*, vol. 61, pp. 239–50, Feb. 2014.

[15] D. T. Yeh *et al.*, "3-D ultrasound imaging using a forward-looking CMUT ring array for intravascular/intracardiac applications," *IEEE Trans. Ultrason. Ferroelect. Freq. Control*, vol. 53, pp. 1202–11, Jun. 2006.

[16] D. N. Stephens *et al.*, "First in vivo use of a capacitive micromachined ultrasound transducer array-based imaging and ablation catheter," *J. Ultrasound Medi.*, vol. 31, pp. 247–256, 2012.

[17] M. Pekař *et al.*, "Preclinical testing of frequency-tunable capacitive micromachined ultrasonic transducer probe prototypes," *Ultrasound Medi. Biol.*, vol. 43, pp. 2079–2085, 2017.

[18] J. Janjic *et al.*, "3D Imaging with a single-element forward-looking steerable IVUS catheter: Initial testing," in *Proc. 2016 IEEE Int. Ultrasonics Symp.*, 2016, pp. 1–4.

[19] J. Janjic *et al.*, "Imaging with a single-element forward-looking steerable IVUS catheter using optical shape sensing," *SPIE Med. Imaging*, 2017, Art. no. 10135-34.

[20] J. D. Scargle, "Studies in astronomical time-series analysis. III-Fourier-transforms, auto-correlation functions, and cross-correlation functions of unevenly spaced data," *Astrophys. J.*, vol. 343, pp. 874–887, Aug. 15, 1989.

[21] D. S. Early and D. G. Long, "Image reconstruction and enhanced resolution imaging from irregular samples," *IEEE Trans. Geosci. Remote Sens.*, vol. 39, no. 2, pp. 291–302, Feb. 2001.

[22] J. G. Bosch *et al.*, "Improved spatiotemporal voxel space interpolation for 3D echocardiography with irregular sampling and multibeat fusion," in *Proc. 2005 IEEE Ultrasonics Symp.*, 2005, vol. 1–4, pp. 1232–1235.

[23] H. Knutsson and C. F. Westin, "Normalized and Differential convolution - methods for interpolation and filtering of incomplete and uncertain data,"in *Proc. 1993 IEEE Comput. Soc. Conf. Comput. Vis. Pattern Recognit.*, 1993, pp. 515–523.

[24] T. Q. Pham and L. J. van Vliet, "Normalized averaging using adaptive applicability functions with applications in image reconstruction from sparsely and randomly sampled data," *Image Anal. Proc.*, vol. 2749, pp. 485–492, 2003.

[25] V. Argyriou *et al.*, "Gradient-adaptive normalized convolution," *IEEE Signal Process. Lett.*, vol. 15, pp. 489–492, 2008.

[26] M. E. Froggatt *et al.*, "Optical position and/or shape sensing," U.S. Patent 8773650, Jul. 8, 2014.

[27] R. G. Duncan *et al.*, "High-accuracy fiber-optic shape sensing - art. no. 65301S," in *Proc. Sensor Syst. Netw., Phenomena, Technol. Appl. NDE Health Monit.*, 2007, vol. 6530, pp. S5301–S5301.

[28] T. L. Szabo, *Diagnostic Ultrasound Imaging: Inside Out*. Burlington, MA, USA: Academic, 2004.